# What Determines the Ice Polymorph in Clouds?

Arpa Hudait and Valeria Molinero*

Department of Chemistry, The University of Utah, 315 South 1400 East, Salt Lake City, Utah 84112-0850, United States

**ABSTRACT:** Ice crystals in the atmosphere nucleate from supercooled liquid water and grow by vapor uptake. The structure of the ice polymorph grown has strong impact on the morphology and light scattering of the ice crystals, modulates the amount of water vapor in ice clouds, and can impact the molecular uptake and reactivity of atmospheric aerosols. Experiments and molecular simulations indicate that ice nucleated and grown from deeply supercooled liquid water is metastable stacking disordered ice. The ice polymorph grown from vapor has not yet been determined. Here we use large-scale molecular simulations to determine the structure of ice that grows as a result of uptake of water vapor in the temperature range relevant to cirrus and mixed-phase clouds,



elucidate the molecular mechanism of the formation of ice at the vapor interface, and compute the free energy difference between cubic and hexagonal ice interfaces with vapor. We find that vapor deposition results in growth of stacking disordered ice only under conditions of extreme supersaturation, for which a nonequilibrium liquid layer completely wets the surface of ice. Such extreme conditions have been used to produce stacking disordered frost ice in experiments and may be plausible in the summer polar mesosphere. Growth of ice from vapor at moderate supersaturations in the temperature range relevant to cirrus and mixed-phase clouds, from 200 to 260 K, produces exclusively the stable hexagonal ice polymorph. Cubic ice is disfavored with respect to hexagonal ice not only by a small penalty in the bulk free energy ($3.6 \pm 1.5$ J mol$^{-1}$ at 260 K) but also by a large free energy penalty at the ice−vapor interface ($89.7 \pm 12.8$ J mol$^{-1}$ at 260 K). The latter originates in higher vibrational entropy of the hexagonal-terminated ice−vapor interface. We predict that the free energy penalty against the cubic ice interface should decrease strongly with temperature, resulting in some degree of stacking disorder in ice grown from vapor in the tropical tropopause layer, and in polar stratospheric and noctilucent clouds. Our findings support and explain the evolution of the morphology of ice crystals from hexagonal to trigonal symmetry with decreasing temperature, as reported by experiments and in situ measurements in clouds. We conclude that selective growth of the elusive cubic ice polymorph by manipulation of the interfacial properties can likely be achieved at the ice−liquid interface but not at the ice−vapor interface.
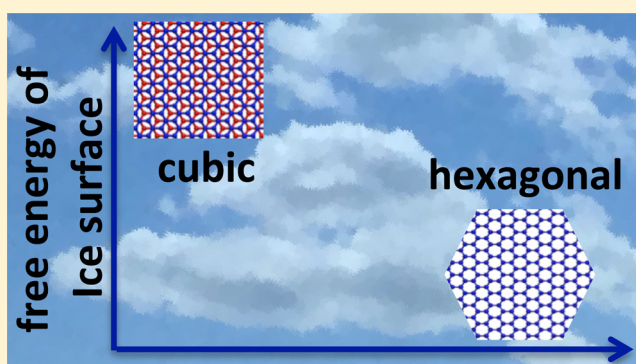
## 1. INTRODUCTION

Ice crystals in the atmosphere are mostly nucleated from supercooled liquid water[1−5] and grown by uptake of water vapor.[6−11] The structure of atmospheric ice is still debated.[12−17] Hexagonal ice (ice I$_h$) is the thermodynamically stable crystal of water at ambient pressures; it consists of identical water layers stacked in the ABABAB sequence perpendicular to the hexagonal axis. Cubic ice (ice I$_c$), a hypothetical metastable polymorph of ice I first proposed by König,[18] instead packs the same layers in the ABCABC sequence. Ice I$_c$ has not yet been synthesized in experiments. The free energy difference between the cubic and hexagonal polymorphs must be less than 8 J mol$^{-1}$,[19] the experimental cost of creating a cubic deformation stacking fault in hexagonal ice.[20] This is supported by simulations with various water models, which predict a free energy difference less than 9 J mol$^{-1}$ between the cubic and hexagonal polymorphs.[21−23] The nucleation and growth of ice from deeply supercooled liquid water results in a metastable stacking disordered polymorph,[12,13,17,24−44] previously misidentified as cubic ice. While plenty of studies have focused on the structure of ices

grown from liquid, little is known about the structure of ices grown from vapor.

Measurements of vapor pressure in ice clouds are usually used to infer the structure of atmospheric ice crystals.[14,15,45] In situ measurements of water vapor in the upper troposphere reported negligible supersaturation with respect to the equilibrium vapor pressure of hexagonal ice in contrail and ice clouds at temperatures above 200 K. Elevated super-saturation was only reported below 200 K.[16,46,47] However, recent measurements in laboratory-created cirrus clouds report saturation vapor pressures matching those of hexagonal ice, without any temperature dependence.[48] It has long been assumed that excess vapor pressure of atmospheric ices is indicative of cubic or stacking disordered ices.[12−15,49] A recent assessment of the free energies of stacking faults and defects in ice, however, indicates that changes in cubicity (fraction of cubic sequences) of ice have very little impact in its vapor pressure.[19] Defects such as ice−liquid and ice−vapor interfaces

may be responsible for the dispersion in vapor pressures observed in ice synthesized from liquid or amorphous ices at very low temperatures.[19] The rare circular Scheiner's halo has been considered as indirect evidence of transient cubic ice in the upper atmosphere[50−52] but could also be due to polycrystalline hexagonal ice.[53] To date there is no direct evidence of cubic ice in the atmosphere, and the structure of atmospheric ice has not yet been fully established.

The structure of the ice polymorph is reflected in the symmetry of the ice crystals. Ice crystals in the atmosphere, as well as those grown from vapor in laboratory above 230 K, are predominantly of hexagonal symmetry, suggesting that the polymorph is ice $I_h$.[7,54,55] Interestingly, a significant fraction of ice crystals of trigonal symmetry is obtained from clouds and laboratory experiments at temperatures below 190 K.[54,56−59] The trigonal morphology of ice crystals in cold clouds has been attributed to the presence of cubic stacking sequences.[57,58] The supersaturation of the vapor likely determines the mechanism of layer formation and may affect the resulting ice polymorph through the kinetics of growth and the thermodynamics of interfaces and defects. It has been suggested that water vapor deposition at screw dislocations in ice results in formation of cubic ice clusters that introduce stacking faults in ice.[60] Indeed, a scanning tunneling microscopy (STM) and atomic force microscopy (AFM) study of ice grown from low supersaturation vapor at 140 K found that cubic ice clusters formed when existing hexagonal clusters coalesced at a screw dislocation.[61] Cubic ice clusters, however, did not nucleate directly from the vapor.[61] The evolution in morphology of ice crystals from hexagonal symmetry at warmer temperatures to trigonal symmetry at colder temperature points to a temperature dependence of the structure of ice grown by vapor uptake.[62,63] In other experiments, stacking disordered frost ice was created at temperatures between 160 and 240 K from vapor at conditions of extreme supersaturation.[12] To date, there has not been yet a direct experimental determination of the polymorphs of ice that grows by uptake of water vapor at atmospherically relevant conditions.

In this work we use large-scale molecular simulations with the computationally efficient mW water model[64] to determine the structure that results when ice is grown from the vapor at temperatures from 200 to 260 K, a range relevant to cirrus and mixed-phase clouds.[65−73] We investigate the mechanism of layer formation in ice and compute the difference in free energy of hexagonal and cubic ice order at the ice−vapor interface. Our results indicate that the crystal that grows by uptake of water vapor in mixed phase and cirrus clouds is hexagonal ice, the stable polymorph. We find that hexagonal ice is not only favored over cubic ice by a small difference in bulk free energy but also by a ∼20 times larger free energy difference, of entropic origin, at the ice−vapor interface.

## 2. METHODS

**2.1. Model and Simulation Settings.** We model water with the monatomic model mW, which represents each water molecule as a single particle that interacts through anisotropic short-range potentials that mimic hydrogen bonds.[64] mW is 180 times computationally more efficient than fully atomistic water models,[64] yet it accurately reproduces the structure of water in the liquid, amorphous, and ice states, as well as the thermodynamics and microscopic mechanisms of crystallization of water and the structure of the premelted layer at the vapor interface.[23,28,29,39−42,64,74−93] mW predicts that hexagonal ice is the most stable bulk ice I polymorph,[23,64] with a melting temperature of 273 ± 0.5 K[20] (see refs 94−96 for the full phase diagram of mW

water) and reproduces the experimental cost of creating a pair of cubic layers in hexagonal ice (8 J mol$^{-1}$ in experiments[20] vs 9.7 ± 1.9 J mol$^{-1}$ in simulations).[19]

All molecular dynamics simulations of this work are performed using LAMMPS.[97] The equations of motion are integrated with the velocity Verlet algorithm using a time step of 10 fs. Periodic boundary conditions are implemented only in the directions of the plane of the ice−vapor interface (the $xy$ plane). The bottom two layers of the ice slabs are fixed to emulate the presence of bulk ice, as previous simulations have shown that the density profile of ice is already bulk-like 10 layers beyond the ice−vapor surface.[92] In the $z$ direction, the cell is nonperiodic; the vapor region is terminated by a reflective wall at about 10 nm from the ice surface. The temperature and pressure are controlled with the Nose−Hoover thermostat and barostat with time scales 25 and 50 ps, respectively, except when otherwise is indicated. The pressures in the $x$ and $y$ directions are controlled independently and set to 1 bar. Because ice has a very low compressibility, the results would be the same if the lateral pressure were set to the vapor pressure (which is 0.5 mbar at 298 K for the mW model and has the same temperature dependence as in the experiment).[98] The rigid part of the slab contracts and expands as a whole in the direction tangential to the ice−vapor interface following the small fluctuations of cell dimensions controlled by the barostat. No barostat is applied in the nonperiodic $z$ direction.

**2.2. Identification of Hexagonal and Cubic Ice at the Ice−Vapor Interface.** We identify ice with the CHILL+ algorithm[99] extended to identify the polymorph of ice for 3-coordinated water molecules at the ice−vapor surface. To identify hexagonal and cubic ice at the ice−vapor interface, we compare the structure of the vapor-exposed layer to the one of the layer below, which we call the template layer. The alignments of two consecutive water layers in a cubic (C) and hexagonal (H) ice interface are shown in Figure 1. We first find all
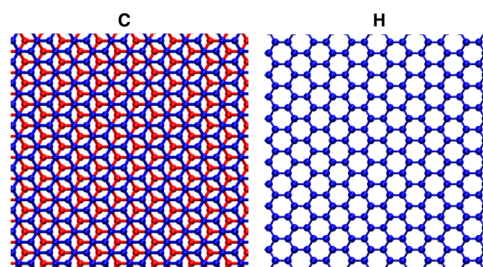


**Figure 1.** Snapshots of two consecutive layers in cubic (left) and hexagonal (right) ices, used to identify the C and H interfaces. The C surface corresponds to the (111) plane of ice $I_c$, whereas the H surface corresponds to the basal or (0001) plane of ice $I_h$. The top layer is shown in blue, and the bottom layer is shown in red. Consecutive water layers are overlaid at the H surface, whereas they are shifted relative to one another in a C surface. Transformation of C to H can be achieved by a collective translation of 2.54 Å of the top layer (blue) relative to the bottom (red) layer.

6-membered water rings in the interfacial layer. This search is restricted to first neighbors, within 3.5 Å, of all the water molecules at the interface. Interfacial water molecules that belong to 6-membered rings are classified as ice and the others as liquid. In the case of hexagonal ice, the molecules that belong to consecutive layers are exactly aligned, and each surface molecule has three aligned neighbors. In cubic ice, there are equal numbers of aligned and unaligned molecules with the underlying layer. We utilize this difference in molecular arrangement to identify cubic and hexagonal order at the ice−vapor interface. First, we loop through all the water molecules that are part of the 6-membered ring to identify if they are aligned with a molecule in the template layer. If we find a molecule in the template layer within 1 Å of the molecule of interest in the $x$ and $y$ plane, we classify it as aligned; otherwise, we classify it as unaligned. A water molecule is considered part of an H surface if the following conditions are satisfied: (1) The central molecule is aligned and has at least two

neighbors that are aligned. (2) Each of the neighbors has at least two neighbors that are aligned including the central molecule. Interfacial cubic ice C consists of both aligned and unaligned molecules. A surface molecule that is aligned is classified as C if the following conditions are satisfied: (1) The molecule of interest has at least two unaligned neighbors. (2) Each of the unaligned neighbors has at least two neighbors that are aligned, including the central molecule. Likewise, a molecule that is unaligned is classified as C if the following conditions are satisfied: (1) The molecule of interest has at least two aligned neighbors. (2) Each of the aligned neighbors has at least two neighbors that are unaligned, including the central molecule.

**2.3. Stability of Ice–Vapor Interfaces.** To investigate the stability of the cubic ice–vapor interface, we evolve molecular dynamics simulations of cubic ice exposing a large area, 21.3 nm × 18.5 nm, of a (111) crystal plane to vacuum at constant temperatures (260, 240, and 220 K) while keeping the pressure at 1 atm in the directions perpendicular to the surface. The ice slabs have 14 water layers, each consisting of 6-membered puckered rings of hydrogen-bonded water molecules in the direction perpendicular to the interface. To assess the stability of cubic ice–vapor interface at lower temperatures, 180 and 200 K, we evolve an interface of the same size with cubic ice present only in a fraction of the surface, with the rest being hexagonal ice. These simulations are evolved in the $NpT$ ensemble for times up to 400 ns.

The potential energy of ice interfaces is computed from simulation cells of ice $I_h$ and ice $I_c$ with 14 layers and an area of 21.3 nm × 18.5 nm in the direction perpendicular to the basal or (111) plane, respectively, to which we add a vacuum slab in the direction perpendicular to the basal or (111) planes. The C layer on top of bulk ice $I_h$ is generated by shifting the top H layer by 2.54 Å (see Figure 1). The energies of the systems are then minimized, and the potential energies of the water molecules at the vacuum interface and the layer below are recorded and averaged per layer. We evolve the slab of cubic ice exposing the (111) plane at 240 K, conditions for which the C termination transforms into the H surface after 10 ns (see section 3.1). From that simulation we compute the average potential energy of the C interfacial layer during the first 10 ns before it converts and the average energy for H during the last 10 ns after it has fully converted.

**2.4. Vapor Deposition.** To investigate the polymorph of ice that results from constant rate molecular dynamics deposition simulations of water in well-defined ice faces, we construct two sizes of simulation cells that expose the basal (0001) plane of hexagonal ice or the (111) plane of cubic ice to the incoming water molecules. The largest cell exposes a surface of area of 21.3 nm × 18.5 nm to the vapor; the smallest exposes a 10 nm × 10 nm area. Both are initially 14 water layers deep, with the two bottom layers fixed. The ice slabs are in contact with a 10 nm thick vapor slab in which water molecules are created at 5.3–5.8 nm above the surface with random initial velocities toward the ice surface that range between 0.35 and 0.85 nm ps$^{-1}$, corresponding to temperatures of the individual molecules between 81 and 521 K, to produce a mean temperature of the deposited molecules close to 300 K. The deposited gas molecules do not have momentum in the $x$ and $y$ direction. The deposition simulations are performed at constant volume and with the temperature controlled by a Nose–Hoover thermostat with a slow relaxation time of 25 ps to allow for flow of thermal energy after each condensation event. Sixteen water molecules are deposited every 100 ps on the large 21.3 nm × 18.5 nm ice surfaces. To analyze the effect of deposition rate, we deposit water molecules in the 10 nm × 10 nm surfaces at rates that range from 4 molecules every 100 ps to 4 molecules every 2 ps.

The average thickness $\delta_{DLL}$ of the nonequilibrium disordered liquid-like layer (DLL) that results from high deposition rates is determined by first computing a histogram of molecules classified as liquid with CHILL+[99] binning the simulation cell in 1 Å slices parallel to the ice–vapor surface. To measure the increased density of liquid due to presence of the DLL, we estimate the full width at half-maximum of the density profile of liquid molecules at the ice–vapor interface at each snapshot and take a time average of the width of the DLL over all the snapshots.

**2.5. Free Energy of Transformation between Hexagonal and Cubic Order at the Ice–Vapor Interface.** To compute the free energy of transformation between H and C states at the ice–vapor interface we investigate two types of systems. The first class of systems consists of an extended ice $I_h$ surface (same as in section 2.4, with 14 layers of ice (bottom two fixed) and with an area of 21.3 nm × 18.5 nm exposed to the vapor) on top of which there is a one-layer disc of ice with a radius of 2.5, 3, or 4 nm (containing 260, 410, and 658 water molecules, respectively) and which is initially in the C configuration with respect to the ice $I_h$ below. We evolve the cell with the smallest disc for 1 $\mu$s at both 260 and 220 K and collect the statistics of the number of H and C molecules in the surface ice cluster every 50 ps, discarding the first 3 ns. The cells with the larger discs were evolved for 200 ns at 260 K. From the population statistics of H and C we compute the 2D probability distribution histogram $P(N_{HEX}, N_{CUB})$, where $N_{HEX}$ and $N_{CUB}$ are the number of water molecules in the disk in hexagonal and cubic ice configurations. The histogram is constructed by binning with $\Delta N = 8$. From this histogram we compute the free energy landscape as the 2D potential of mean force (PMF):

$$\Delta G(N_{HEX}, N_{CUB}) = -RT \ln P(N_{HEX}, N_{CUB}) \tag{1}$$

where $R$ is the universal gas constant and $T$ is the temperature. We use the same procedure to investigate the relative stabilities of H and C surfaces for the second ice–vapor surface: a periodic ice $I_h$ slab with 14 ice layers (bottom two fixed) and a 4.6 nm × 5.3 nm basal area (~280 water molecules) exposed to vacuum. We evolve this simulation cell for 18 $\mu$s at 260 K, computing the number of molecules with the order of cubic ice, hexagonal ice, and liquid at the surface every 50 ps. We compute the PMF for the first and second half of the 18 $\mu$s simulation and report the average as the free energy and half the difference as the error bar.

## 3. RESULTS AND DISCUSSION

**3.1. Ice Grown from the Vapor Is the Stable, Hexagonal Polymorph.** We perform large-scale simulations of growth of ice exposing the basal plane using constant deposition rate simulations at 220, 240, and 260 K, the temperature range relevant for ice crystal growth in cirrus and mixed-phase clouds. Under these conditions, all thermalized water molecules that reach the surface of ice stick to it, in agreement with previous simulations.[100,101] The slowest rate of uptake used in this study is 1.17 cm s$^{-1}$, which corresponds to 0.4 molecules deposited per nm$^2$ ns (i.e., it takes 25 ns to build a single layer of ice in the simulation slab that exposes an area of 395 nm$^2$). This rate of deposition is much faster than expected from experimental vapor pressures; it would take ~10 $\mu$s to grow a single layer of ice in the simulation cells at the experimental equilibrium vapor pressure at 260 K[14] and even longer at lower temperatures. Growing ice at a deposition rate that would correspond to the experimental vapor pressure is computationally impractical, even with the very efficient water model of this work.

The simulations show that water vapor uptake at 220, 240, and 260 K always results in growth of hexagonal ice, regardless of whether the substrate is the cubic or hexagonal polymorph. The processes of formation of a new layer at 260 and 220 K are illustrated in Figure 2. Water molecules deposited on top of a complete ice layer diffuse through the surface and coalesce into one layer thick small clusters. These ice islands grow by accretion of individual molecules and by consolidation with other islands. In agreement with optical microscopy experiments,[102,103] we do not observe the formation of multilayer clusters at the surface.

Deposition at relatively warm temperatures, 240 and 260 K, results in small surface clusters that fluctuate between liquid
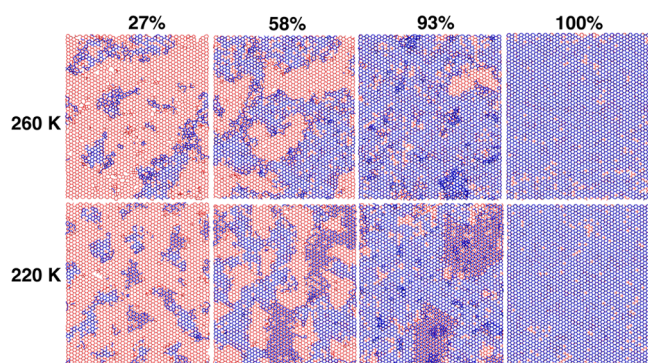
**Figure 2.** Progression of formation of a new ice layer by deposition of water vapor at 260 and 220 K at 27, 58, 93, and 100% completion. The new water layer is represented with blue sticks, and the ice layer below is represented with red sticks. Small C clusters exist in the initial stages of deposition at 260 K, but only H order remains when the deposition of a layer is complete (100%). C clusters survive to larger sizes along the deposition process at 220 K, and they are still noticeable when the system reaches 100% coverage. However, C patches continue to transform into H order even as new layers are deposited on top, resulting in the fully hexagonal layer shown here.

(L), cubic (C), and hexagonal (H) order by small collective translation of the molecules during the initial stages of layer formation. The collective fluctuations between H and C order become increasingly rare as the clusters grow larger. For example, surface clusters with more than 350 molecules are primarily comprised of hexagonal ice in equilibrium with liquid at the island boundary, while the occurrence of cubic ice is rare and short-lived. As the ice islands grow, they always favor the H interfacial order, which grows into a full H layer by adsorption of water from the vapor (Figure 2). The result is that ice grown from the vapor at relatively warm temperatures is exclusively hexagonal.

Deposition of vapor at 220 K also results in small C and H clusters. Different from the evolution at warmer temperatures, at 220 K the C and H orders do not interconvert in the time scales of the deposition: the clusters grow in size forming contiguous C and H islands mediated by contact lines made of 5-, 7-, and 8-membered rings[19,30,77] (see lower panels of Figure 2). Transformation of C to H at these cold temperatures occurs not by the nucleation of H order in C clusters observed at the warmer temperatures but through displacement and reduction of the contact line between neighboring C and H domains. The final result of vapor deposition at relatively cold and warm temperatures is nevertheless identical: the growth of hexagonal ice layers.

To address whether the surface of ice would be purely hexagonal at the even lower temperatures relevant for cirrus clouds,[104−106] we prepare hexagonal ice exposing to vacuum a basal plane that was initially 45% C and 55% H. The transformation of all cubic order the surface into H takes less than 0.5 $\mu$s at 200 K, significantly less than the time required to deposit this layer with the vapor pressures occurring in the atmosphere. The C → H transformation is slower at 180 K; nevertheless, we observe an advance in the conversion of C to H within hundreds of nanoseconds. We conclude that at temperatures relevant for cirrus cloud formation growth of ice by vapor uptake from high supersaturation environments will result in the stable crystal polymorph.

The results above indicate that a hexagonal-terminated ice interface is more stable than a cubic-terminated one. To

provide insight on the degree of metastability of cubic terminated interfaces, we investigate the C → H transformation starting from large, periodically replicated, all-C surfaces on top of ices $I_c$ and $I_h$ at temperatures relevant to ice or mixed-phase clouds, from 260 to 200 K. We find that a C interface is effectively unstable at 260 K, irrespective of the substrate polymorph: the all-C layer transforms immediately (within 1 ns in the simulations) into an H layer by a process akin to spinodal decomposition. This implies that the nucleation barrier between the C and H states at 260 K is lower than or comparable to the thermal energy. Free energy calculations in section 3.2 verify this interpretation. At 240 K (Figure 3), the C
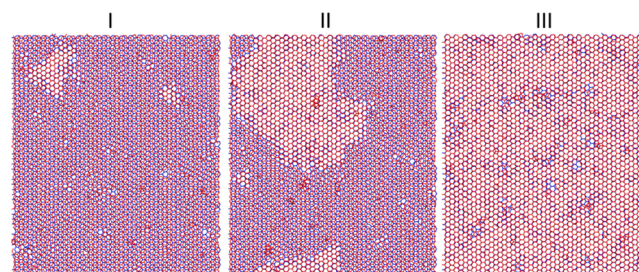


**Figure 3.** Transformation of a cubic layer C on top of $I_c$ into a hexagonal layer H at 240 K by nucleation and growth of patches of hexagonal order. The snapshots I−III display the upper two layers in the system after 12, 23, and 50 ns of the simulation, respectively, that starts with an all-C surface. The upper layer is represented with blue sticks, and the layer below is represented with red sticks. The supercritical hexagonal patch (seen first in panel I) grows (panel II) until the transformation to a hexagonal surface is complete (panel III).

→ H transformation occurs through nucleation and growth of H patches, with a short induction period of about 10 ns. Defects consisting of coupled 5-, 7-, and 8-membered rings, which have been previously reported to form at the boundaries between C and H order within an ice layer,[19,30,77] first appear in the top C layer and surround the patches of H order within the outermost layer of ice. The H patches in the top ice layer are short-lived during the induction period (see subcritical H patches in panel I of Figure 3). Eventually, an H patch of critical size forms and grows, irreversibly transforming the upper layer of ice from C to H order (Figure 3, panels II and III). At temperatures of 220 K and colder, the induction period to produce critical-sized hexagonal patches is too long for our simulations; however, we have shown above that when H and C surface patches are in coexistence at 220 and 200 K, there is an irreversible transformation toward an all-H interface. These results imply that even if cubic interfaces were to form (e.g., by growth of stacking disordered ice from supercooled liquid or at a screw dislocation), the exposition of a cubic terminated ice surface to the vapor would result in an irreversible albeit may be very slow transformation to a hexagonal interface.

It may be expected that if ice were grown from vapor with a rate of water deposition higher than the rate of accommodation of the molecules into the crystal structure, a disordered nonequilibrium liquid layer would form on the surface of ice. This poses the question of whether ice covered with a disordered liquid-like layer grows stacking disordered, as is the case for ice grown from deeply supercooled liquid water in experiments.[13,19,28,29,76,81] In previous work we showed that the ratio of cubic to hexagonal layers in ice grown from liquid is mostly controlled by kinetics, but it is also modulated by the small free energy preference for hexagonal ice in the bulk[23,29,64]

and at the ice—liquid interface.[19] Here we grow ice from vapor at increasingly higher rates of deposition to investigate whether under any circumstance the resulting ice is stacking disordered. Figure 4 shows that when the deposition rate is so fast that the
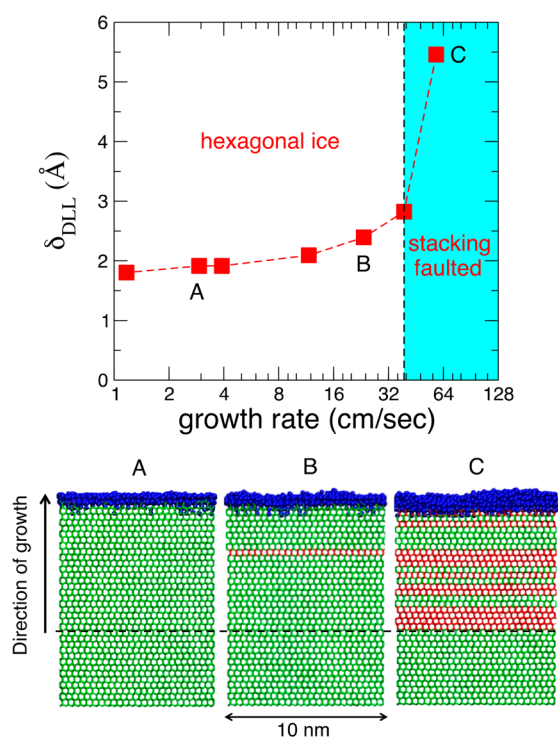


**Figure 4.** Upper panel: Average width of the nonequilibrium disordered liquid layer ($\delta_{DLL}$) on ice that results by water uptake on the basal plane at 260 K, as a function of growth (deposition) rate. $\delta_{DLL}$ increases with the rate of water deposition. When $\delta_{DLL}$ reaches a value larger than a water diameter (~0.3 nm), the ice surface is covered by liquid, and the ice grows stacking faulted (cyan area in the figure). The lower panel shows snapshots of ice grown from vapor at the rates indicated as A, B, and C in the upper panel. Bonds in hexagonal and cubic ice are shown with green and red respectively, and liquid is represented as blue balls. The area of growth is $10 \times 10$ nm$^2$; 20 new layers (above the dashed line) are grown in these simulations. A is grown at a rate of 3 cm s$^{-1}$ and results in purely hexagonal ice, B at a rate of 23.4 cm s$^{-1}$ and produces 5% cubic layers, and C at a rate of 58.5 cm s$^{-1}$ and results in 55% cubic layers. The stacking disordered ice grown at the fastest deposition rate of this study has random cubic and hexagonal sequences and is qualitatively similar to the ice grown from ice exposing the basal plane of hexagonal ice to supercooled liquid water.[13,19,24]

entire ice surface is covered by disordered water, ice grows with stacking faults. Under those conditions, a new layer is not formed by nucleation of islands in contact with vapor but from the nonequilibrium disordered layer, akin to growth of ice from liquid.[19,24,30−32,74,107,108] A vapor supersaturation of about 16 000 would be needed to reach that scenario. Such extreme supersaturations are unlikely in the troposphere. However, supersaturations up to $10^6−10^8$, forced by gravity waves, are thought to be possible in the summer polar mesosphere.[109,110] Our results suggest that the growth of ice crystals under conditions of extreme supersaturation in the summer polar mesosphere will result in stacking disordered ice. Extreme supersaturations can also be achieved in laboratory experiments. Growth of frost ice at conditions of very high supersaturation results in stacking disordered ice,[12,111] in

agreement with our simulations. In next section we show that for atmospherically relevant conditions for which the crystal surface is exposed to vapor, growth of hexagonal ice from vapor is promoted not only by a very slow rate of growth that favors the stable polymorph but also by a strong free energy penalty against cubic ice at the ice—vapor interface, about 25 times larger than the penalty against cubic ice at the ice—liquid interface.[19]

**3.2. Thermodynamic Preference for Hexagonal Order at the Vapor Interface Is Entropy Driven.** To understand the extent by which the ice—vapor interface favors hexagonal order, and the origin of this preference, we compute the free energy of the transformation between cubic and hexagonal order for two type of interfaces: (i) one-layer thick discs of ice on top of an ice $I_h$ slab and (ii) the periodic surface of an ice $I_h$ slab. The discs in the first case represent ice islands in the initial stages of layer formation, while the second case corresponds to a fully formed, complete ice surface. To collect the statistics from which we derive the free energy, we evolve long simulations of one-layer thick ice clusters of radii 2.5, 3, and 4 nm on top of the surface of ice $I_h$ at 260 K, and we compute the probability distributions of cubic, hexagonal, and liquid order in these clusters as a function of time. All surface discs transform from their initial all-C order to H order with a liquid boundary extremely quickly, within 1 ns. This transformation is achieved through small translation of the molecules (see Figure 1). The clusters fluctuate in shape and exchange water molecules with the underlying ice but always remain single-layer, as we observed in the deposition simulations of section 3.1. Of the three cluster sizes we study at 260 K, only the smaller one (radius 2.5 nm, with 260 water molecules) occasionally reverts back to predominantly C order over a 1 $\mu$s simulation (Figure 5). Even then, the transformation into C is not complete; patches of liquid water always surround the ice (see snapshots in Figure 6).

We compute the free energy landscape for the surface ice disk as a function of the number of molecules with cubic order, $N_{CUB}$, and hexagonal order, $N_{HEX}$, using the histograms of populations of cubic ($N_{CUB}$) and hexagonal ($N_{HEX}$) ice collected over the 1 $\mu$s simulation of the 2.5 nm disc on ice
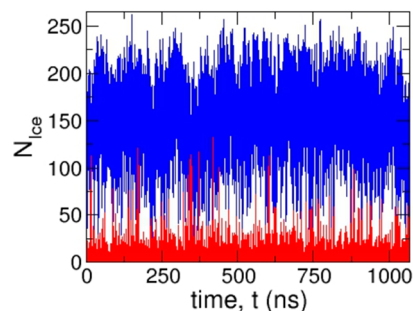


**Figure 5.** Evolution of the number of molecules with cubic (red) and hexagonal (blue) ice order in a 2.5 nm radius disk at the interface between hexagonal ice and vapor. The disk contains 260 water molecules; liquid-like molecules of the disk (those that are not C or H) are not shown in the plot. The surface disc is prepared as all C and transforms to an H disk with liquid-like boundaries within 1 ns of the simulation (not shown). The disc remains predominantly H throughout the 1 $\mu$s time evolution with a small amount of C. The C-rich cluster is smaller than the H-rich cluster (i.e., the C and H order coexist with different amount of liquid-like order), and its formation is a rare event.
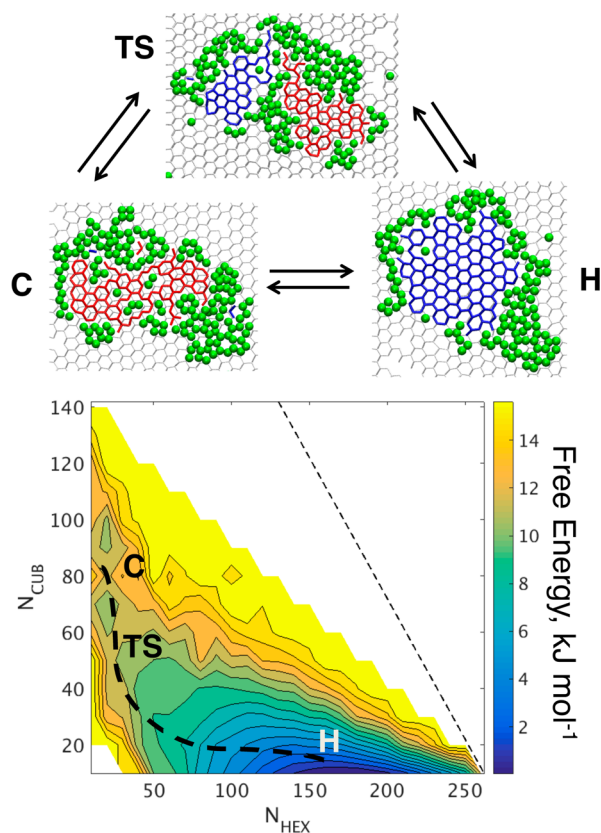
**Figure 6.** Upper panel: Representative structures of the C, H, and TS configurations. The underlying hexagonal ice surface is shown with gray bonds, the hexagonal order in the cluster is shown with blue bonds, the cubic order is shown with red bonds, and noncrystalline molecules in the clusters are represented with green balls. The transition state (TS) configurations contains C and H patches in coexistence, separated by a line of defects consisting of coupled 5-, 7-, and 8-membered rings and surrounded by disordered liquid-like water. The free energy barrier that separates the C- and H-rich basins is controlled by the difference in free energy between cubic and hexagonal ice at the surface and the line tension of the C−H boundary within the cluster and increases with cluster size,[19] which is why the transformation is difficult to sample for large clusters with brute force simulations. Lower panel: Free energy landscape for the surface disc of radius 2.5 nm at 260 K. C and H in the landscape point to the local free energy minima of the C- and H-rich clusters, respectively. The transition state (TS) signals the top of the free energy barrier that connects (dashed line) C and H states in the surface cluster. The cubic region (C) consists of two minima instead of one continuous minimum because of insufficient sampling of the C basin. The dotted line shows the relation expected between $N_{CUB}$ and $N_{HEX}$ if there were no liquid molecules in the cluster.

$I_h$ at 260 K shown in Figure 5. The free energy landscape (Figure 6) displays two minima: a broad deep well corresponding to predominantly hexagonal ice order surrounded by liquid-like water (about 135−210 H molecules out of the 260 in the cluster) and a shallower minimum corresponding to about 60−105 molecules with C order surrounded by liquid. The free energy difference between these two minima is 10 kJ per mole of surface discs, in favor of the H-rich order. These results indicate that the formation of predominantly hexagonal ice clusters in the early stage of layer formation (Figure 2) is due to their higher thermodynamic stability.

Because the C- and H-rich basins of the free energy landscape of the disk on top of ice $I_h$ have a different number of liquid-like waters (Figure 6), we cannot extract from these simulations the free energy cost of transforming a surface water molecule from hexagonal to cubic order. To overcome this issue, we evolve a periodic slab of hexagonal ice that exposes to vacuum the basal plane with ∼280 molecules and which has an area per cell comparable to the one of the disc of Figures 5 and 6. Different from the transformation pathway in the disc, the transformation in the periodic surface conserves the amount of liquid-like water (i.e., the extent of premelting of the surface) at the C and H basins. We evolve the periodic ice−vapor surface at 260 K for 18 $\mu$s to compute the free energy landscape as a function of $N_{CUB}$ and $N_{HEX}$ (Figure 7) and extract the free energy difference between cubic and hexagonal order at the vapor interface.
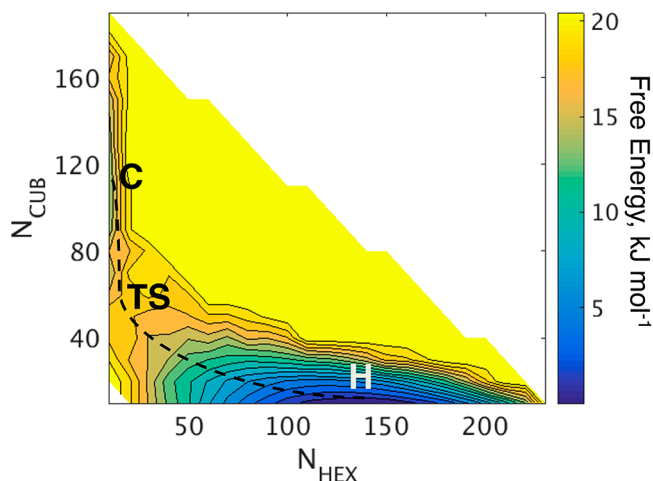


**Figure 7.** Free energy landscape of transformation of a periodic basal surface of hexagonal ice exposed to vapor at 260 K, computed from 18 $\mu$s long simulations. The transformation between hexagonal (H) and cubic (C) order at the surface occurs via nucleation and growth, as illustrated in Figure 3. Defects consisting of coupled 5-, 7-, and 8-membered rings and disordered, liquid-like water consist of around 20% of the molecules at the ice−vapor interface and facilitate the nucleation of the new surface order. Different from the results shown for the surface cluster in Figure 6, the C and H basins of the periodic surface contain the same number of ice molecules. The barrier between the C and H basins in the free energy landscape is controlled by the line tension between C and H in the same plane and the difference in free energy between C and H at the interface[19] and would increase with the dimensions of the cell.

The structure of the interface of the periodic ice slab evolves slowly, by appearance and disappearance of small patches of cubic order, along the 18 $\mu$s of the simulation. Only rarely (15 times in 18 $\mu$s), a critical patch of C order nucleates and grows a cubic ice surface, which rapidly returns to a hexagonal surface. The free energy landscape (Figure 7) displays two minima corresponding to the C and H order, each consisting of about 140 molecules. The hexagonal ice termination is thermodynamically more stable than the cubic ice termination at the ice−vapor interface by 99.7 ± 12.6 J mol$^{-1}$ (48.5 ± 6.1 J mol$^{-1}$ or 0.9 mJ m$^{-2}$ when all molecules at the interface, including those premelted, are considered). The 99.7 ± 12.6 J mol$^{-1}$ free energy difference between C and H at the vapor interface is the sum of three contributions: (i) the bulk free energy difference between cubic and hexagonal ice, $\Delta G_{I_c - I_h}$ = 4.4 ± 1.5 J mol$^{-1}$ at

260 K,[23] (ii) the free energy cost of creating an interface between a cubic and a hexagonal layer, $\Delta G_{sf}$ = 5.6 ± 1.2 J mol$^{-1}$,[19] and (iii) the difference in free energy between a cubic ice−vapor and a hexagonal ice−vapor interface, $\Delta G_{C/vapor-H/vapor}$ = (99.7 ± 12.6 − 4.4 ± 1.5 − 5.6 ± 1.2) J mol$^{-1}$ = 89.7 ± 12.8 J mol$^{-1}$. The penalty against cubic ice at the ice−vapor interface is 25 times larger than the one at the ice−liquid interface, $\Delta G_{I_c/liquid-I_h/liquid}$ = 3.8 ± 1.8 J mol$^{-1}$.[19]

The high free energy penalty of a cubic termination at the ice−vapor interface is mostly entropic: the difference in potential energy between a C and H terminated surface with vapor contributes only 0.9 J mol$^{-1}$ at 0 K and is indistinguishable from 0 at 240 K. Neglecting the enthalpic contribution, we estimate the difference in entropy against the cubic interface at 260 to be $\Delta S_{C/vapor-H/vapor} \approx -\Delta G_{C/vapor-H/vapor}/T$ = −0.35 J K mol$^{-1}$. We note that the difference in entropy between the cubic and hexagonal surface is less than 2% of the one between ice and liquid water at the melting temperature (19.25 J K mol$^{-1}$ for mW water,[75] in good agreement with the 22.0 J K mol$^{-1}$ experimental value).[112] As mW water does not have rotational degrees of freedom, $\Delta S_{C/vapor-H/vapor}$ must originate on a higher vibrational entropy of the hexagonal interface. A recent DFT study of the relative stability of bulk cubic and hexagonal ice attributed the higher stability of hexagonal ice to more anharmonic O−H vibrational modes in ice $I_h$ than in ice $I_c$.[113] The mW model correctly predicts that bulk ice $I_h$ is more stable than bulk ice $I_c$ and reproduces the experimental cost of creating a stacking fault, the thermodynamics of ice melting, and the ice−liquid and liquid−vapor surface tensions.[19,23,64,114] However, it may underestimate the destabilization of cubic ice at the vapor interface because the only vibrational contribution in the mW model is from O−O (or center of mass) vibrations. It is an open question whether differences in vibrational density of states of the under-coordinated O−H bonds at the ice surface magnify the free energy difference between hexagonal and cubic terminated ice−vapor surfaces beyond the value predicted by mW model. Future calculations with fully atomistic flexible models are needed to assess the contribution of water rotations and O−H vibrations to the free energy difference between cubic and hexagonal ice at the vapor interface.

The presence of structural defects in ice can alter the morphology of the crystals.[57] Hexagonal ice crystals have hexagonal symmetry.[7] Ice crystals with trigonal symmetry have been observed in the atmosphere, most prominently at temperatures below 190 K.[56,57,59] The trigonal symmetry has been attributed to the presence of cubic stacking faults in hexagonal ice.[25,56,57,115] Cubic ice layers have been observed in ice deposited from vapor at temperatures below 150 K.[61,116] In these experiments, hexagonal ice steps first nucleate and grow at the ice surface, and cubic ice can form upon coalescence of these steps at a screw dislocation. The experimental free energy cost of dislocation in ice is 78 J mol$^{-1}$ in the temperature range of 150−180 K.[117] We expect the free energy cost of a dislocation to be dominated by enthalpy and not very temperature-dependent. The cost of the cubic-terminated interface is 89.7 ± 12.8 J mol$^{-1}$ at 260 K and it should decrease strongly with temperature because of its entropic origin. On the basis of these results, at temperatures below ∼200 K, the per-molecule cost of a dislocation should be higher than the free energy cost of a cubic−vapor interface. A compromise between these two defects may explain the

formation of cubic ice at the site of dislocations in experiments at 150 K.[61] Propagation of cubic ice away from the dislocation should increase the free energy according to the amount of cubic ice exposed to vapor ($N_{C/vapor} \times \Delta G_{C/vapor-H/vapor}$) and the number $N_{CH}$ of molecules at the in-layer defective line that connects cubic and hexagonal order in a plane ($N_{CH} \times \Delta G_{CH}$, where $\Delta G_{CH}$ is 130 ± 15 J mol$^{-1}$).[19] The combined free energy contributions from all these factors suggests that even though the dislocation can initiate the growth of cubic ice in thermodynamic equilibrium the ice layer will anneal to hexagonal ice away from the dislocation. At very low temperatures, however, it may take a longer time to achieve equilibrium than to grow a new layer of ice on top of the exposed cubic layer. The latter would decrease the driving force of the transformation to H order because the cost of the stacking interface ($\Delta G_{sf}$ = 5.6 ± 1.2 J mol$^{-1}$[119]) is over an order of magnitude lower than $\Delta G_{C/vapor-H/vapor}$. On the basis of these arguments and the results of this work, we expect a very small fraction of cubic layers in ice grown from vapor, even at the lowest temperatures for ice formation in the troposphere. That small fraction of cubic sequences could be responsible for the trigonal symmetry of the ice crystal. An experimental characterization of the density of stacking faults of ice crystals grown from vapor is needed to conclusively determine the relation between cubicity and morphology of atmospheric ice crystals.

## 4. CONCLUSIONS

In this work we use large-scale molecular dynamics simulation with the mW water model to determine (i) the structure of ice that grows through vapor uptake from 200 to 260 K, a temperature range relevant to cirrus or mixed-phase clouds in Earth's atmosphere, (ii) the mechanism of formation of new ice layers by vapor deposition, and (iii) the magnitude and physical origin of the free energy difference between cubic- and hexagonal-terminated ice interfaces exposed to the vapor.

The simulations indicate that vapor uptake results in growth of hexagonal ice in the entire temperature range relevant for mixed-phase and cirrus clouds. This prediction agrees with the predominantly hexagonal morphology of ice crystals grown from vapor in experiments above 230 K.[7,54,55] The formation of a new ice layer in the simulations proceeds via nucleation and growth of single-layered clusters, as previously observed in optical microscopy experiments.[102,103] We find that small single-layered clusters of ice fluctuate between cubic and hexagonal order by collective translation in the early stages of layer formation. As the area of the clusters increase, these fluctuations become rare, and the clusters remain predominantly in the hexagonal ice order. Our simulations agree with AFM-STM experiments of vapor deposition at cold temperatures, which indicate that only hexagonal clusters are nucleated at the ice surface,[61] and demonstrate that the mechanism of layer formation remains the same at warm temperatures.

Stacking disordered ice grows from vapor in simulations only under extreme supersaturations for which the rate of water deposition is higher than the rate of its accommodation into the crystal lattice. Such extreme supersaturations are plausible in the summer polar mesosphere and can also be achieved in laboratory experiments of frost formation from vapor, which indeed produce stacking disordered ices.[12,118] Under these conditions, the simulations indicate that a nonequilibrium disordered layer completely wets the ice surface. This creates a liquid−ice interface, which favors hexagonal ice relative to cubic

ice by only a small free energy difference, $3.8 \pm 1.8$ J mol$^{-1}$.[19] Our results show that liquid-like disorder at the ice surface can result in formation of stacking faults in ice grown from vapor. Stacking faults by themselves, however, add little to the free energy of ice (8 J mol$^{-1}$ in experiments[20] and $9.7 \pm 1.9$ J mol$^{-1}$ in simulations with the mW model[19]) and cannot be responsible for a significant increase in the vapor pressure. Defects such as porosity and grain boundaries that create high free energy ice−vapor and ice−liquid interfaces[19] could be primary contributors to supersaturation in ice clouds and contrails.

The simulations reveal that the ice−vapor interface favors hexagonal over cubic order by a free energy difference of $\Delta G_{\text{C/vapor−H/vapor}} = 89.7 \pm 12.8$ J mol$^{-1}$ at 260 K ($48.5 \pm 6.1$ J mol$^{-1}$ or 0.9 mJ m$^{-2}$ if the premelted water at the ice−vapor surface is also counted). The penalty against cubic ice at the vapor interface is over 20 times higher than at the liquid interface[19] and in bulk.[23] Our analysis indicates that the difference in enthalpy between the cubic and hexagonal interfaces is negligible and that $\Delta G_{\text{C/vapor−H/vapor}}$ originates in a larger entropy of the hexagonal interface. Hence, $\Delta G_{\text{C/vapor−H/vapor}} \approx -T\Delta S_{\text{C/vapor−H/vapor}}$ and should decrease strongly on cooling. The lower penalty against cubic ice−vapor interfaces at low temperatures, along with a slow kinetics for the transformation of metastable cubic interfaces, may facilitate the formation of cubic ice clusters at screw dislocations in experiments below 150 K.[61] Our analysis suggests that persistent cubic ice sequences could be found in noctilucent clouds, where temperatures are as low as 100 K,[58,110,119,120] and supports the existence of some extent of stacking disorder in ice grown from vapor below 190 K and in the tropical tropopause layer and polar stratospheric clouds, where trigonal ice crystals were found.[56−59]

The entropy difference between the surfaces of hexagonal and cubic ice in contact with vapor should be reflected in distinct density of states of vibrational modes for these two surfaces. The mW water model can only account for contributions arising from the O−O (or center of mass) vibrational modes and may underestimate the free energy penalty against cubic ice. Flexible polarizable water models that are built from first-principles, such as MB-Pol[121] (which was recently used to predict the vibrational spectrum at the liquid−vapor interface in excellent agreement with experiment[122]) would be ideal to evaluate the differences in vibrational density of states of cubic and hexagonal ice interfaces exposed to vapor. Identification of the vibrational modes that destabilize a cubic interface is key to develop surface additives that can tilt the free energy stability in favor of the cubic interface. In that quest, it is worthwhile looking into the behavior of compounds of the periodic groups IV and III−V, which share with water the formation of tetrahedrally coordinated crystal polymorphs.[64,123,124] Diamond cubic is the stable polymorph of group IV silicon and germanium and of III−V (e.g., GaAs, InP) semiconductors, whereas the hexagonal diamond structure is metastable. The expected difference in free energy between cubic and hexagonal polymorph in silicon is significantly larger than that in water.[125] However, the metastable hexagonal polymorph of silicon and other tetrahedrally coordinated semiconductors have been recently realized by controlling growth conditions: temperature, supersaturation, and chemical composition of the vapor.[126−128] Polymorph selection against the stable bulk crystal polymorph by interfacial molecules has also been reported in the biomineralization of calcium

carbonate,[129−132] as well as pharmaceuticals and other organic crystals.[133−136] We hypothesize that it may be possible to synthesize the elusive cubic ice polymorph by controlling the interfacial energy through additives that direct the polymorph selection. We note that heterogeneous nucleation of ice in molecular simulations has resulted in selective nucleation and growth of specific polymorphs or facets of ice depending on the nucleating surface.[78,79,137−139] Manipulation of the ice−liquid interface, which has a penalty against cubic order 25 times smaller than the ice−vapor interface, may offer the most promising avenue to synthesize cubic ice in laboratory experiments.

## ■ AUTHOR INFORMATION

### Corresponding Author
*E-mail: Valeria.Molinero@utah.edu.

### Notes
The authors declare no competing financial interest.

## ■ REFERENCES

(1) Kerminen, V.-M.; Wexler, A. S.; Potukuchi, S. *J. Geophys. Res.* **1997**, *102*, 3715.
(2) Heymsfield, A. J.; Miloshevich, L. M.; Schmitt, C.; Bansemer, A.; Twohy, C.; Poellot, M. R.; Fridlind, A.; Gerber, H. *J. Atmos. Sci.* **2005**, *62*, 41−64.
(3) Heymsfield, A. J.; Miloshevich, L. M. *J. Atmos. Sci.* **1993**, *50*, 2335−2353.
(4) Rogers, D. C.; DeMott, P. J.; Kreidenweis, S. M.; Chen, Y. *Geophys. Res. Lett.* **1998**, *25*, 1383−1386.
(5) Murray, B. J.; O'Sullivan, D.; Atkinson, J. D.; Webb, M. E. *Chem. Soc. Rev.* **2012**, *41*, 6519−6554.
(6) Lamb, D.; Hobbs, P. V. *J. Atmos. Sci.* **1971**, *28*, 1506−1509.
(7) Libbrecht, K. G. *Rep. Prog. Phys.* **2005**, *68*, 855−895.
(8) Westbrook, C. D.; Heymsfield, A. J. *J. Atmos. Sci.* **2011**, *68*, 2416−2429.
(9) Libbrecht, K. G. *arXiv:1110.5828 [cond-mat.mtrl-sci]* 2012.
(10) Gonda, T.; Koike, T. *J. Cryst. Growth* **1982**, *56*, 259−264.
(11) Comstock, J. M.; Lin, R.-F.; Starr, D. O. C.; Yang, P. *J. Geophys. Res.* **2008**, *113*, D23211.
(12) Kuhs, W. F.; Sippel, C.; Falenty, A.; Hansen, T. C. *Proc. Natl. Acad. Sci. U. S. A.* **2012**, *109*, 21259−21264.
(13) Malkin, T. L.; Murray, B. J.; Salzmann, C. G.; Molinero, V.; Pickering, S. J.; Whale, T. F. *Phys. Chem. Chem. Phys.* **2015**, *17*, 60−76.
(14) Murphy, D. M.; Koop, T. *Q. J. R. Meteorol. Soc.* **2005**, *131*, 1539−1565.
(15) Shilling, J. E.; Tolbert, M. A.; Toon, O. B.; Jensen, E. J.; Murray, B. J.; Bertram, A. K. *Geophys. Res. Lett.* **2006**, *33*, L17801.
(16) Jensen, E. J.; Smith, J. B.; Pfister, L.; Pittman, J. V.; Weinstock, E. M.; Sayres, D. S.; Herman, R. L.; Troy, R. F.; Rosenlof, K.; Thompson, T. L.; Fridlind, A. M.; Hudson, P. K.; Cziczo, D. J.; Heymsfield, A. J.; Schmitt, C.; Wilson, J. C. *Atmos. Chem. Phys.* **2005**, *5*, 851−862.
(17) Murray, B. J.; Knopf, D. A.; Bertram, A. K. *Nature* **2005**, *434*, 202−205.
(18) König, H. *Z. Kristallogr.* **1944**, *105*, 279−286.
(19) Hudait, A.; Qiu, S.; Lupi, L.; Molinero, V. *Phys. Chem. Chem. Phys.* **2016**, *18*, 9544−9553.
(20) Hondoh, T.; Itoh, T.; Amakai, S.; Goto, K.; Higashi, A. *J. Phys. Chem.* **1983**, *87*, 4040−4044.

(21) Zaragoza, A.; Conde, M. M.; Espinosa, J. R.; Valeriani, C.; Vega, C.; Sanz, E. *J. Chem. Phys.* **2015**, *143*, 134504.

(22) Smallenburg, F.; Poole, P. H.; Sciortino, F. *Mol. Phys.* **2015**, *113*, 2791−2798.

(23) Quigley, D. *J. Chem. Phys.* **2014**, *141*, 121101.

(24) Carignano, M. A. *J. Phys. Chem. C* **2007**, *111*, 501−504.

(25) Hansen, T. C.; Koza, M. M.; Kuhs, W. F. *J. Phys.: Condens. Matter* **2008**, *20*, 285104.

(26) Hansen, T. C.; Koza, M. M.; Lindner, P.; Kuhs, W. F. *J. Phys.: Condens. Matter* **2008**, *20*, 285105.

(27) Malkin, T. L.; Murray, B. J.; Brukhno, A. V.; Anwar, J.; Salzmann, C. G. *Proc. Natl. Acad. Sci. U. S. A.* **2012**, *109*, 1041−1045.

(28) Moore, E. B.; de la Llave, E.; Welke, K.; Scherlis, D. A.; Molinero, V. *Phys. Chem. Chem. Phys.* **2010**, *12*, 4124−4134.

(29) Moore, E. B.; Molinero, V. *Phys. Chem. Chem. Phys.* **2011**, *13*, 20008−20016.

(30) Pirzadeh, P.; Kusalik, P. G. *J. Am. Chem. Soc.* **2011**, *133*, 704−707.

(31) Choi, S.; Jang, E.; Kim, J. S. *J. Chem. Phys.* **2014**, *140*, 014701.

(32) Seo, M.; Jang, E.; Kim, K.; Choi, S.; Kim, J. S. *J. Chem. Phys.* **2012**, *137*, 154503.

(33) Murray, B. J.; Bertram, A. K. *Phys. Chem. Chem. Phys.* **2008**, *10*, 3287−3301.

(34) Murray, B. J. *Environ. Res. Lett.* **2008**, *3*, 025008.

(35) Salzmann, C. G.; Mayer, E.; Hallbrucker, A. *Phys. Chem. Chem. Phys.* **2004**, *6*, 1269−1276.

(36) Kuhs, W.; Bliss, D.; Finney, J. *J. Phys. Colloq.* **1987**, *48*, C1-631−C1-636.

(37) Morishige, K.; Yasunaga, H.; Uematsu, H. *J. Phys. Chem. C* **2009**, *113*, 3056−3061.

(38) Mayer, E.; Hallbrucker, A. *Nature* **1987**, *325*, 601−602.

(39) Reinhardt, A.; Doye, J. P. K. *J. Chem. Phys.* **2012**, *136*, 054501.

(40) González Solveyra, E.; De La Llave, E.; Scherlis, D. A.; Molinero, V. *J. Phys. Chem. B* **2011**, *115*, 14196−14204.

(41) Moore, E. B.; Allen, J. T.; Molinero, V. *J. Phys. Chem. C* **2012**, *116*, 7507−7514.

(42) Moore, E. B.; Molinero, V. *J. Chem. Phys.* **2009**, *130*, 244505.

(43) Haji-Akbari, A.; Debenedetti, P. G. *Proc. Natl. Acad. Sci. U. S. A.* **2015**, *112*, 10582−10588.

(44) Sosso, G. C.; Li, T.; Donadio, D.; Tribello, G. A.; Michaelides, A. *J. Phys. Chem. Lett.* **2016**, 2350−2355.

(45) Peter, T.; Marcolli, C.; Spichtinger, P.; Corti, T.; Baker, M. B.; Koop, T. *Science* **2006**, *314*, 1399−1402.

(46) Krämer, M.; Schiller, C.; Afchine, A.; Bauer, R.; Gensch, I.; Mangold, A.; Schlicht, S.; Spelten, N.; Sitnikov, N.; Borrmann, S.; De Reus, M.; Spichtinger, P. *Atmos. Chem. Phys.* **2009**, *9*, 3505−3522.

(47) Spichtinger, P.; Gierens, K.; Read, W. *Q. J. R. Meteorol. Soc.* **2003**, *129*, 3391−3410.

(48) Lamb, K.; Clouser, B.; Sarkozy, L.; Wagner, S.; Ebert, V.; Kerstel, E.; Saathoff, H.; Möhler, O.; Moyer, E. *EGU General Assembly Conference Abstracts* **2015**, *17*, 15244.

(49) Murphy, D. M. *Geophys. Res. Lett.* **2003**, *30*, 2230−2230.

(50) Riikonen, M.; Sillanpää, M.; Virta, L.; Sullivan, D.; Moilanen, J.; Luukkonen, I. *Appl. Opt.* **2000**, *39*, 6080.

(51) Tape, W. *Atmospheric Halos, Vol. 64 of Antarctic Research Series* (American Geophysical Union, 1994).

(52) Whalley, E. *J. Phys. Chem.* **1983**, *87*, 4174−4179.

(53) Weinheimer, A. J.; Knight, C. A. *J. Atmos. Sci.* **1987**, *44*, 3304−3308.

(54) Bailey, M.; Hallett, J. *J. Atmos. Sci.* **2004**, *61*, 514−544.

(55) Mason, B. J. *Q. J. R. Meteorol. Soc.* **1994**, *120*, 849−860.

(56) Heymsfield, A. J. *J. Atmos. Sci.* **1986**, *43*, 851−855.

(57) Murray, B. J.; Salzmann, C. G.; Heymsfield, A. J.; Dobbie, S.; Neely, R. R.; Cox, C. J. *Bull. Am. Meteorol. Soc.* **2015**, *96*, 1519−1531.

(58) Murray, B. J.; Malkin, T. L.; Salzmann, C. G. *J. Atmos. Sol.-Terr. Phys.* **2015**, *127*, 78−82.

(59) Lawson, R. P.; Pilson, B.; Baker, B.; Mo, Q.; Jensen, E.; Pfister, L.; Bui, P. *Atmos. Chem. Phys.* **2008**, *8*, 1609−1620.

(60) Wood, S. E.; Baker, M. B.; Calhoun, D. *J. Geophys. Res.* **2001**, *106*, 4845−4870.

(61) Thurmer, K.; Nie, S. *Proceedings of the National Academy of Sciences,* *110*, 11757−11762.

(62) Yamashita, A. *J. Meteorol. Soc. Jpn.* **1973**, *51*, 307−317.

(63) Yamashita, A. *J. Meteorol. Soc. Jpn.* **1971**, *49*, 215−231.

(64) Molinero, V.; Moore, E. B. *J. Phys. Chem. B* **2009**, *113*, 4008−4016.

(65) Korolev, A. V.; Isaac, G. A.; Cober, S. G.; Strapp, J. W.; Hallett, J. *Q. J. R. Meteorol. Soc.* **2003**, *129*, 39−65.

(66) Lawson, R. P.; Gettelman, A. *Proc. Natl. Acad. Sci. U. S. A.* **2014**, *111*, 18156−18161.

(67) Morrison, H.; de Boer, G.; Feingold, G.; Harrington, J.; Shupe, M. D.; Sulia, K. *Nat. Geosci.* **2011**, *5*, 11−17.

(68) Rosenfeld, D.; Woodley, W. L. *Nature* **2000**, *405*, 440−442.

(69) Sun, Z.; Shine, K. P. *Q. J. R. Meteorol. Soc.* **1994**, *120*, 111−137.

(70) Cziczo, D. J.; Froyd, K. D.; Hoose, C.; Jensen, E. J.; Diao, M.; Zondlo, M. A.; Smith, J. B.; Twohy, C. H.; Murphy, D. M. *Science* **2013**, *340*, 1320−1324.

(71) Rollins, A. W.; Thornberry, T. D.; Gao, R. S.; Woods, S.; Lawson, R. P.; Bui, T. P.; Jensen, E. J.; Fahey, D. W. *Geophys. Res. Lett.* **2016**, *43*, 2912−2918.

(72) Taylor, J. R.; Randel, W. J.; Jensen, E. J. *Atmos. Chem. Phys.* **2011**, *11*, 10085−10095.

(73) Wang, M.; Penner, J. E. *Atmos. Chem. Phys.* **2010**, *10*, 5449−5474.

(74) Moore, E. B.; Molinero, V. *J. Chem. Phys.* **2010**, *132*, 244504.

(75) Moore, E. B.; Molinero, V. *Nature* **2011**, *479*, 506−508.

(76) Johnston, J. C.; Molinero, V. *J. Am. Chem. Soc.* **2012**, *134*, 6650−6659.

(77) Nguyen, A. H.; Koc, M. A.; Shepherd, T. D.; Molinero, V. *J. Phys. Chem. C* **2015**, *119*, 4104−4117.

(78) Lupi, L.; Hudait, A.; Molinero, V. *J. Am. Chem. Soc.* **2014**, *136*, 3156−3164.

(79) Lupi, L.; Kastelowitz, N.; Molinero, V. *J. Chem. Phys.* **2014**, *141*, 18C508.

(80) Lupi, L.; Molinero, V. *J. Phys. Chem. A* **2014**, *118*, 7330−7337.

(81) Hudait, A.; Molinero, V. *J. Am. Chem. Soc.* **2014**, *136*, 8081−8093.

(82) Bullock, G.; Molinero, V. *Faraday Discuss.* **2014**, *167*, 371−388.

(83) Kastelowitz, N.; Johnston, J. C.; Molinero, V. *J. Chem. Phys.* **2010**, *132*, 124511.

(84) Limmer, D. T.; Chandler, D. *J. Chem. Phys.* **2012**, *137*, 044509.

(85) Holten, V.; Limmer, D. T.; Molinero, V.; Anisimov, M. A. *J. Chem. Phys.* **2013**, *138*, 174501.

(86) Limmer, D. T.; Chandler, D. *J. Chem. Phys.* **2014**, *141*, 18C505.

(87) Li, T.; Donadio, D.; Russo, G.; Galli, G. *Phys. Chem. Chem. Phys.* **2011**, *13*, 19807−19813.

(88) Li, T.; Donadio, D.; Galli, G. *Nat. Commun.* **2013**, *4*, 1887.

(89) Xu, L.; Molinero, V. *J. Phys. Chem. B* **2011**, *115*, 14210−14216.

(90) DeMille, R. C.; Cheatham, T. E.; Molinero, V. *J. Phys. Chem. B* **2011**, *115*, 132−142.

(91) Lu, J.; Qiu, Y.; Baron, R.; Molinero, V. *J. Chem. Theory Comput.* **2014**, *10*, 4104−4120.

(92) Shepherd, T. D.; Koc, M. A.; Molinero, V. *J. Phys. Chem. C* **2012**, *116*, 12172−12180.

(93) Limmer, D. T.; Chandler, D. *arXiv preprint arXiv:1407.3514* **2014**.

(94) Romano, F.; Russo, J.; Tanaka, H. *Physical Review B - Condensed Matter and Materials Physics* **2014**, *90*.

(95) Jacobson, L. C.; Hujo, W.; Molinero, V. *J. Phys. Chem. B* **2009**, *113*, 10298−10307.

(96) Lu, J.; Chakravarty, C.; Molinero, V. *J. Chem. Phys.* **2016**, *144*, 234507.

(97) Plimpton, S. *J. Comput. Phys.* **1995**, *117*, 1−19.

(98) Factorovich, M. H.; Molinero, V.; Scherlis, D. A. *J. Chem. Phys.* **2014**, *140*, 064111.

(99) Nguyen, A. H.; Molinero, V. *J. Phys. Chem. B* **2015**, *119*, 9369−9376.

(100) Batista, E. R.; Ayotte, P.; Bilić, A.; Kay, B. D.; Jónsson, H. *Phys. Rev. Lett.* **2005**, *95*, 223201.

(101) Pfalzgraff, W.; Neshyba, S.; Roeselová, M. *J. Phys. Chem. A* **2011**, *115*, 6184−6193.

(102) Sazaki, G.; Asakawa, H.; Nagashima, K.; Nakatsubo, S.; Furukawa, Y. *Cryst. Growth Des.* **2014**, *14*, 2133−2137.

(103) Sazaki, G.; Zepeda, S.; Nakatsubo, S.; Yokoyama, E.; Furukawa, Y. *Proc. Natl. Acad. Sci. U. S. A.* **2010**, *107*, 19702−19707.

(104) Heymsfield, A.; Winker, D.; Avery, M.; Vaughan, M.; Diskin, G.; Deng, M.; Mitev, V.; Matthey, R. *J. Appl. Meteor. Clim.* **2014**, *53*, 479−505.

(105) Spichtinger, P.; Krämer, M. *Atmos. Chem. Phys.* **2013**, *13*, 9801−9818.

(106) Hoyle, C. R.; Engel, I.; Luo, B. P.; Pitts, M. C.; Poole, L. R.; Grooß, J. U.; Peter, T. *Atmos. Chem. Phys.* **2013**, *13*, 9577−9595.

(107) Rozmanov, D.; Kusalik, P. G. *J. Chem. Phys.* **2012**, *137*, 094702.

(108) Rozmanov, D.; Kusalik, P. G. *Phys. Chem. Chem. Phys.* **2011**, *13*, 15501−15511.

(109) Murray, B. J.; Jensen, E. J. *J. Atmos. Sol.-Terr. Phys.* **2010**, *72*, 51−61.

(110) Lübken, F. J.; Lautenbach, J.; Höffner, J.; Rapp, M.; Zecha, M. *J. Atmos. Sol.-Terr. Phys.* **2009**, *71*, 453−463.

(111) Kuhs, W. F.; Genov, G.; Staykova, D. K.; Hansen, T. *Phys. Chem. Chem. Phys.* **2004**, *6*, 4917−4920.

(112) CRC-Handbook *Handbook of Chemistry and Physics*; CRC: Boca Raton, 2000−2001; Vol. 81th ed..

(113) Engel, E. A.; Monserrat, B.; Needs, R. J. *Phys. Rev. X* **2015**, *5*, 021003.

(114) Baron, R.; Molinero, V. *J. Chem. Theory Comput.* **2012**, *8*, 3696−3704.

(115) Yamashita, A. *J. Meteorol. Soc. Jpn.* **1973**, *51*, 307−317.

(116) Maier, S.; Lechner, B. A. J.; Somorjai, G. A.; Salmeron, M. *J. Am. Chem. Soc.* **2016**, *138*, 3145−3151.

(117) Hondoh, T. *Philos. Mag.* **2015**, *95*, 3590−3620.

(118) Falenty, A.; Genov, G.; Hansen, T. C.; Kuhs, W. F.; Salamatin, A. N. *J. Phys. Chem. C* **2011**, *115*, 4022−4032.

(119) Lübken, F. J. *J. Geophys. Res.* **1999**, *104*, 9135−9149.

(120) Seele, C.; Hartogh, P. *Geophys. Res. Lett.* **1999**, *26*, 1517−1520.

(121) Babin, V.; Leforestier, C.; Paesani, F. *J. Chem. Theory Comput.* **2013**, *9*, 5395−5403.

(122) Medders, G. R.; Paesani, F. *J. Am. Chem. Soc.* **2016**, *138*, 3912−3919.

(123) Angell, C. A.; Bressel, R. D.; Hemmati, M.; Sare, E. J.; Tucker, J. C. *Phys. Chem. Chem. Phys.* **2000**, *2*, 1559−1566.

(124) Hujo, W.; Shadrack Jabes, B.; Rana, V. K.; Chakravarty, C.; Molinero, V. *J. Stat. Phys.* **2011**, *145*, 293−312.

(125) Raffy, C.; Furthmüller, J.; Bechstedt, F. *Phys. Rev. B: Condens. Matter Mater. Phys.* **2002**, *66*, 075201.

(126) Joyce, H. J.; Wong-Leung, J.; Gao, Q.; Tan, H. H.; Jagadish, C. *Nano Lett.* **2010**, *10*, 908−915.

(127) Joyce, H. J.; Gao, Q.; Tan, H. H.; Jagadish, C.; Kim, Y.; Fickenscher, M. A.; Perera, S.; Hoang, T. B.; Smith, L. M.; Jackson, H. E.; Yarrison-Rice, J. M.; Zhang, X.; Zou, J. *Nano Lett.* **2009**, *9*, 695−701.

(128) Hauge, H. I. T.; Verheijen, M. A.; Conesa-Boj, S.; Etzelstorfer, T.; Watzinger, M.; Kriegner, D.; Zardo, I.; Fasolato, C.; Capitani, F.; Postorino, P.; Kölling, S.; Li, A.; Assali, S.; Stangl, J.; Bakkers, E. P. A. M. *Nano Lett.* **2015**, *15*, 5855−5860.

(129) Belcher, A. M.; Wu, X. H.; Christensen, R. J.; Hansma, P. K.; Stucky, G. D.; Morse, D. E. *Nature* **1996**, *381*, 56−58.

(130) Kun Park, H.; Lee, I.; Kim, K. *Chem. Commun.* **2004**, 24−25.

(131) Bano, A. M.; Rodger, P. M.; Quigley, D. *Langmuir* **2014**, *30*, 7513−7521.

(132) Freeman, C. L.; Harding, J. H.; Quigley, D.; Rodger, P. M. *Angew. Chem., Int. Ed.* **2010**, *49*, 5135−5137.

(133) Chen, S.; Xi, H.; Yu, L. *J. Am. Chem. Soc.* **2005**, *127*, 17439−17444.

(134) Mitchell, C. A.; Yu, L.; Ward, M. D. *J. Am. Chem. Soc.* **2001**, *123*, 10830−10839.

(135) Price, C. P.; Grzesiak, A. L.; Matzger, A. J. *J. Am. Chem. Soc.* **2005**, *127*, 5512−5517.

(136) Tao, J.; Jones, K. J.; Yu, L. *Cryst. Growth Des.* **2007**, *7*, 2410−2414.

(137) Zielke, S. A.; Bertram, A. K.; Patey, G. N. *J. Phys. Chem. B* **2015**, *119*, 9049−9055.

(138) Zielke, S. A.; Bertram, A. K.; Patey, G. N. *J. Phys. Chem. B* **2016**, *120*, 2291−2299.

(139) Cox, S. J.; Raza, Z.; Kathmann, S. M.; Slater, B.; Michaelides, A. *Faraday Discuss.* **2014**, *167*, 389−403.